Supporting Information:

Ultrahigh Mass Activity for Carbon Dioxide Reduction Enabled by Gold-iron Core-shell Nanoparticles

Kun Sun, [†, ‡] Tao Cheng, [⊥, ‡] Lina Wu, [∥] Yongfeng Hu, [§] Jigang Zhou, [§] Aimee Maclennan, [§] Zhaohua Jiang, [†] Yunzhi Gao, [†] William A. Goddard III[*, ⊥], and Zhijiang Wang[*, †]

[†] MIIT Key Laboratory of Critical Materials Technology for New Energy Conversion and Storage, School of Chemistry and Chemical Engineering, Harbin Institute of Technology, Harbin 150001, China.

[⊥] Materials and Process Simulation Center (MSC) and Joint Center for Artificial Photosynthesis (JCAP), California Institute of Technology, Pasadena, California 91125, United States.

[∥] Department of Radiology, Molecular Imaging Research Center of Harbin Medical University, the Fourth Hospital of Harbin Medical University, Harbin 150001, China.

[§] Canadian Light Source Inc., Saskatoon, Saskatchewan S7N 0X4, Canada.

*Correspondence to wag@wag.caltech.edu and wangzhijiang@hit.edu.cn;.

Materials and Methods

Materials

All materials, including iron (III) acetylacetonate, 1,2-hexadecanediol, octyl ether, oleylamine, oleic acid, hexane, ethanol, were purchased from Sigma-Aldrich, except gold (III) acetate from Alfa Aesar, and were used as received without further processing. Au foil (99.95% metal basis) was purchased from Alfa Aesar. Carbon black was obtained from Cabot Corporation. Ultrapure water was from a Millipore Autopure system.

Synthesis of AuFe-NPs

Au-Fe nanoalloys were synthesized by the one-pot wet chemical approach. In a typical experiment, $Fe(acac)_3$ (12.5 mM), $Au(OOCCH_3)_3$ (37.5 mM) and the reduction agent of 1,2-hexadecanediol (250 mM) were dissolved in 10 ml octyl ether solution with oleic acid (25 mM) and oleyl amine (25 mM). Under vigorous stirring and Ar atmosphere, the reaction mixture was first heated to 80 ºC and homogenized at that temperature for 1 h, then rapidly raised to 280 ºC and refluxed for 1 h to complete the reaction. Subsequently, ethanol was added into the reacted mixture to precipitate the formed nanoparticles (NPs) after cooling down to room temperature. The resulting dark-red product was separated from the supernatant by centrifugation and washed with mixed ethanol/hexane solvents (1:2) twice and redispersed in hexane.

Synthesis of Au NPs

8-nm sized Au NPs were synthesized similar with AuFe-NPs but without the iron salt in the solution.

Characterizations

X-ray diffraction (XRD) patterns of the samples were recorded on a Bruker AXS D5000 diffractometer. Transmission electron microscope (TEM) images were obtained on a Tecnai G2 F30 electron microscope under an accelerating voltage of 300 keV. TEM samples were prepared by dropping a diluted suspension onto amorphous carbon-coated copper grids and drying in the air. X-ray photoelectron spectroscopy (XPS) of samples was measured using a PHI 5700 X-ray photoelectron spectrometer equipped with a monochromatic Al Kα X-ray source. Inductive coupled plasma atomic emission spectrometry (ICP-AES) analysis carried on a PE OPTIMA5300DV spectrometer was used to characterize the metal quantity in Au-Fe

nanoalloys and in the electrolyte after electrolysis. X-ray absorption spectroscopy (XAS) measurements for the samples were carried out in fluorescence mode using IDEAS beamline at the Canadian Light Source (CLS).

Preparation of working electrode

Au-Fe alloy NPs were deposited onto Cabot carbon black by sonicating the mixture of Au-Fe alloy NPs dispersion in hexane and carbon black. To dry and remove the surfactant, the C-AuFe was annealed overnight in a vacuum-oven at 180 °C. Then, 5 mg of the powders were mixed with 950 μL ethanol and 50 μL 5 wt% Nafion solution by sonication for 0.5 h to form a homogeneous ink. Subsequently, 5 μL suspension was drop-dried onto a glassy carbon electrode.

Electrochemical Measurements

All electrochemical experiments were performed in a three-electrode system using a Autolab Potentiostat. An airtight two-compartment electrochemical cell was separated by an anion exchange membrane with 0.5 M $KHCO_3$ electrolyte (pH 7.2) in each chamber. The electrolyte in the cathodic compartment was stirred magnetically at a rate of 1000 rpm during electrolysis. A piece of platinum wire was used as the counter electrode. All potentials were measured against an Ag/AgCl reference electrode (3.0 M KCl) and converted to the reversible hydrogen electrode (RHE) reference scale using

$$E\ (\text{vs RHE}) = E\ (\text{vs Ag/AgCl}) + 0.210 + 0.0591 \times \text{pH} \quad \text{(S1)}$$

Before electrolysis, the electrolyte in the cathodic compartment was bubbled with CO_2 gas for 1 h. A steady supply of CO_2 gas was delivered at a rate of 20.0 sccm. The cathode compartment was vented directly into the sampling loop of a gas chromatograph (GC, Aglient 7890A). The GC analysis was set up to split the gas sample into two aliquots. One aliquot passed a thermal conductivity detector (TCD), and the other was routed through flame ionization detector (FID). ^{1}H NMR was employed to test for possible liquid-phase products. Their concentration was analyzed on Bruker Avance 400 MHz spectrometer. All potentials were *iR*-corrected. The electrochemically active surface area is determined by Pb UPD experiment.

The Faradaic efficiency and partial current of H_2 and CO production ($FE_{H2\ or\ CO}$ and $i_{H2\ or\ CO}$) were calculated from GC chromatogram peak areas where $V_{H2\ or\ CO}$ is volume concentration of H_2 or CO based on the calibration of the GC. The equation is as following.

$$i_{H_2 or\ CO} = V_{H_2\ or\ CO} \times Q \times \frac{2Fp_0}{RT} \quad \text{(S2)}$$

$$FE_{H_2 or\ CO} = \frac{i_{H_2\ or\ CO}}{i_{total}} \times 100 \quad \text{(S3)}$$

$$mass\quad activity = \frac{FE_{CO} \times i_{total}}{\beta m_{cat}} \quad \text{(S4)}$$

where i_{total} is measured current, F is Faradaic constant, p_0 is pressure, T is temperature and R is ideal gas constant, 8.314 J mol K^{-1}, β is Au or Au-Fe weight ratio in total carbon-supported NP catalysts, m_{cat} is catalyst weight

Computational details

The QM calculations were carried out using the VASP software [1-3], using the PBE flavor[4] of DFT. The projector augmented wave (PAW) method[5] was used to account for core-valence interactions. The kinetic energy cutoff for plane wave expansions was set to 400 eV, and reciprocal space was sampled by Γ-centered Monkhorst-Pack scheme with a grid of 5×5×1. The 2×2 slabs of Au-Metal subsurface model were constructed with 4 layers (bottom layer fixed) using optimized cell parameters of 3:1 Au-metal bulk phase, respectively. The vacuum layer is at least 15 Å above the surface. The convergence criteria are 1×10^{-7} eV energy differences for solving the electronic wavefunction. The Methfessel-Paxton smearing of second order with a width of 0.1 eV was applied. All geometries (atomic coordinates) were converged to within 1×10^{-2} eV/Å for maximal components of forces. In the calculation of CO2 binding energies, a post-stage vdW DFT-D3 method with Becke-Jonson damping was applied.[6] The TS search was conducted with using climbing image nudged elastic band (CI-NEB) method.[7]

$$E_{*\mathrm{COOH}}^{\mathrm{Formation}} = E_{*\mathrm{COOH}} - \left(E_{*} + E_{\mathrm{CO_2}} + \frac{E_{\mathrm{H_2}}}{2}\right) \quad \text{(S5)}$$

$$E_{\mathrm{CO}}^{\mathrm{Desorption}} = \left(E_{*} + E_{\mathrm{CO}}\right) - E_{*\mathrm{CO}} \quad \text{(S6)}$$

$$E_{*\mathrm{CO_2}}^{\mathrm{Adsorption}} = E_{*\mathrm{CO_2}} - \left(E_{*} + E_{\mathrm{CO_2}}\right) \quad \text{(S7)}$$

$$E_{*\mathrm{H}}^{\mathrm{Adsorption}} = E_{*\mathrm{H}} - \left(E_{*} + \frac{E_{\mathrm{H_2}}}{2}\right) \quad \text{(S8)}$$

The Gibbs free energies were calculated at 298 K and 1 atm as outlined in (S5):

$$G = H - T\Delta S = E_{DFT} + E_{ZPE} + E_{solv} + \int_{0}^{298} C_v dT - T\Delta S \quad \text{(S9)}$$

where E_{DFT} is the DFT-optimized total energy, E_{ZPE} is the zero-point vibrational energy, E_{solv} is the solvation energy. $\int_{0}^{298} C_v dT$ is the heat capacity, T is the temperature, and ΔS is the entropy. Gas-phase molecules such as CO_2 and H_2 were treated using the ideal gas approximation, whereas adsorbents were treated using a harmonic approximation. The solvation was treated implicitly using the CANDLE method[8] using the JDFTx simulation package. The GBRV[9] ultrasoft pseudopotentials (USPP) were used, with a plane wave cutoff of 544 eV (20 a.u.). All other settings are similar to those in VASP calculations. We assume variations in these corrections are small compared to variations in adsorbate binding energies and apply the corrections calculated for Au(111) to all adsorbates.

Supporting Figures

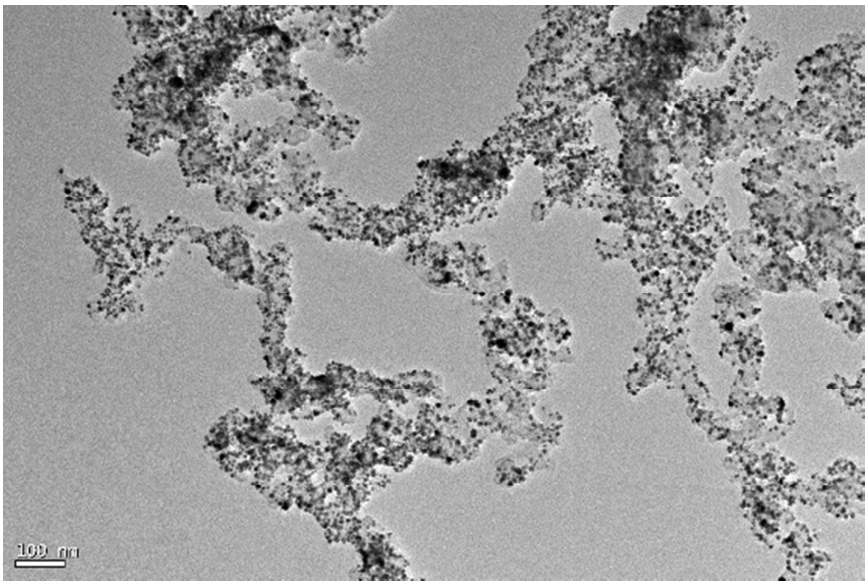

Figure S1. Low resolution TEM image of prepared AuFe-NPs. Scale bar is 100 nm.

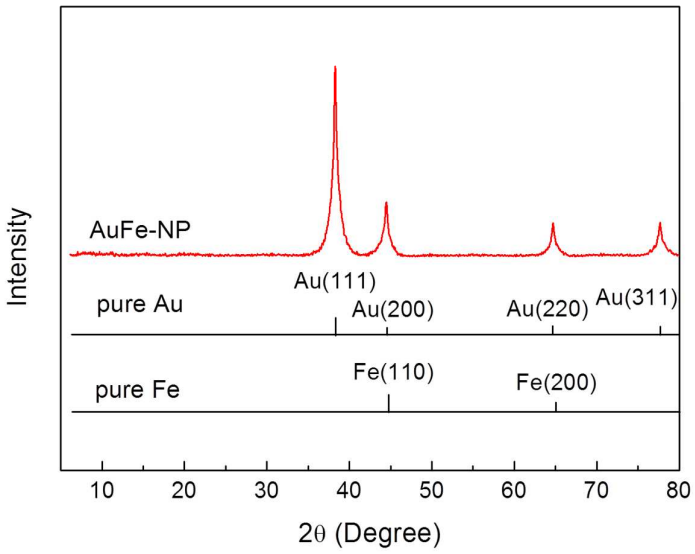

Figure S2. XRD pattern of freshly prepared Au-Fe alloy NPs.

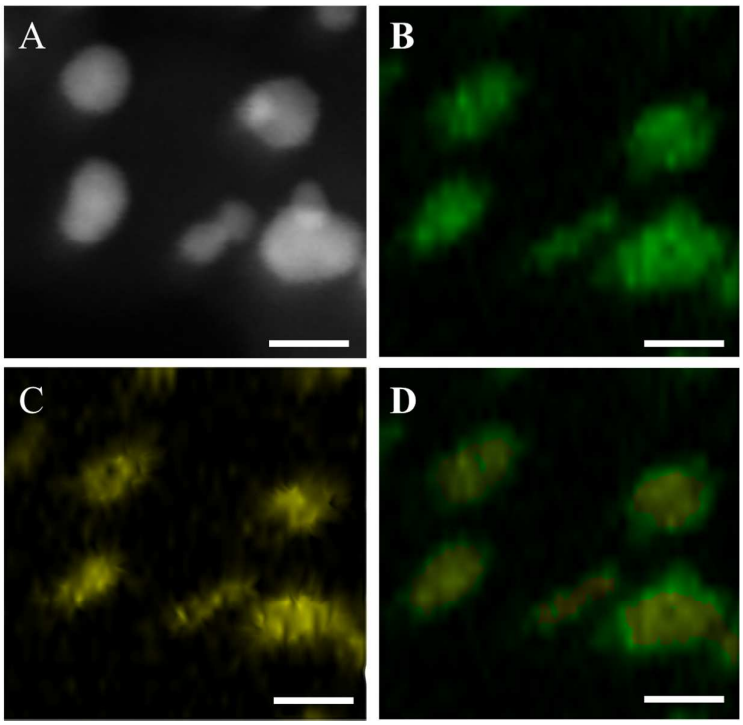

Figure S3. STEM image of AuFe-CSNPs after 12-hours' electrolysis (A) and their corresponding EDX elemental map (B-D); (B) Au element mapping image, (C) Fe element mapping image, (D) merging Au and Fe in one image. Scale bar is 10 nm.

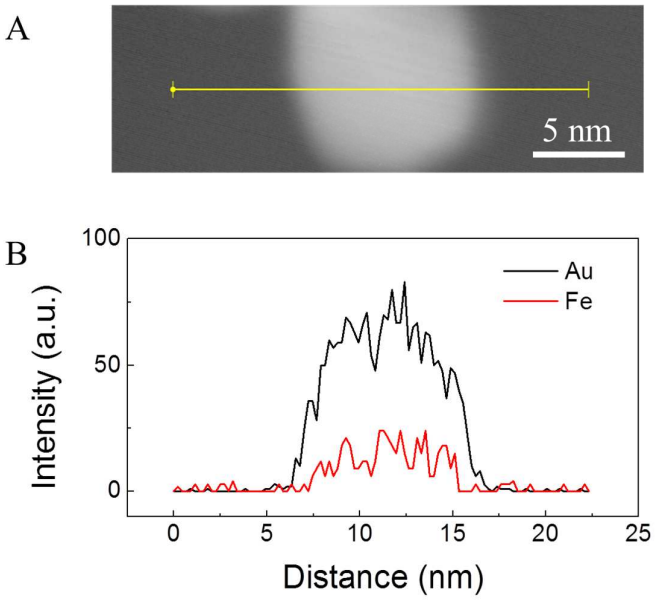

Figure S4. STEM image of one AuFe-CSNP (A) and its corresponding line scan EDX elemental analysis (B).

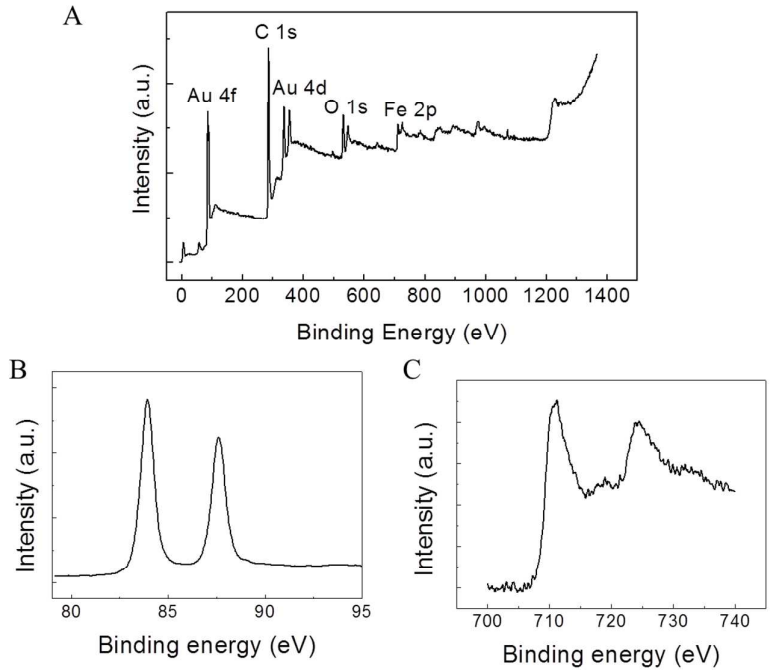

Figure S5. XPS spectra of AuFe-NPs. (A) full-range XPS spectrum; (B) Au 4*f* XPS spectrum; (C) Fe 3*d* XPS spectrum.

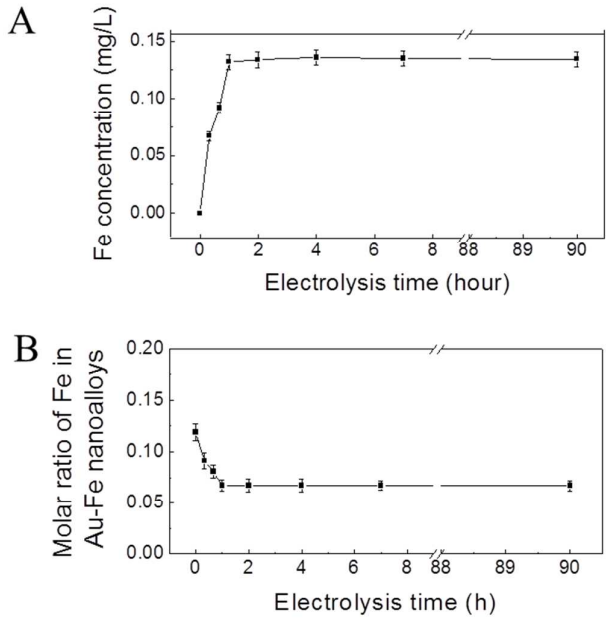

Figure S6. Variation of Fe concentration measured by ICP-AES with the electrolysis time. (A) the Fe content in electrolyte vs. electrolysis time, and (B) molar ratio of Fe in AuFe-NP vs. electrolysis time.

As shown in Figure S6, Fe leaching takes place in the first hour electrolysis in electrolyte of CO_2-saturated 0.5 M $KHCO_3$ (pH 7.2). The Fe concentration increases quickly during the initial hour of the electrolysis time (Figure S6A). Then, the Fe concentration in electrolyte remains constant, indicating that the AuFe-NPs have completed the surface reconstruction and reached stable state. This was confirmed by the molar concentration for Fe in nanoalloy obtained from ICP-AES (Figure S6B).

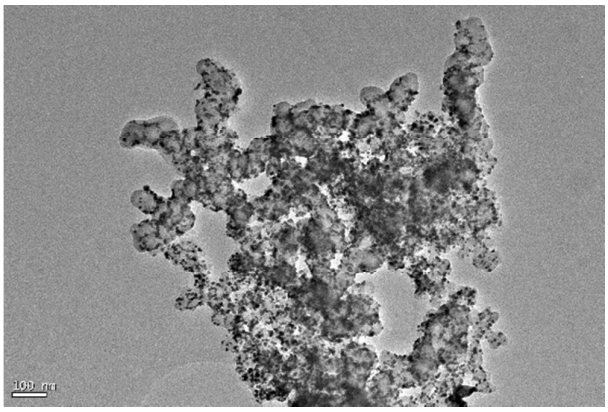

Figure S7. Low resolution TEM image of AuFe-CSNPs, which are formed by AuFe-NPs undergone surface Fe leaching out. Scale bar is 100 nm.

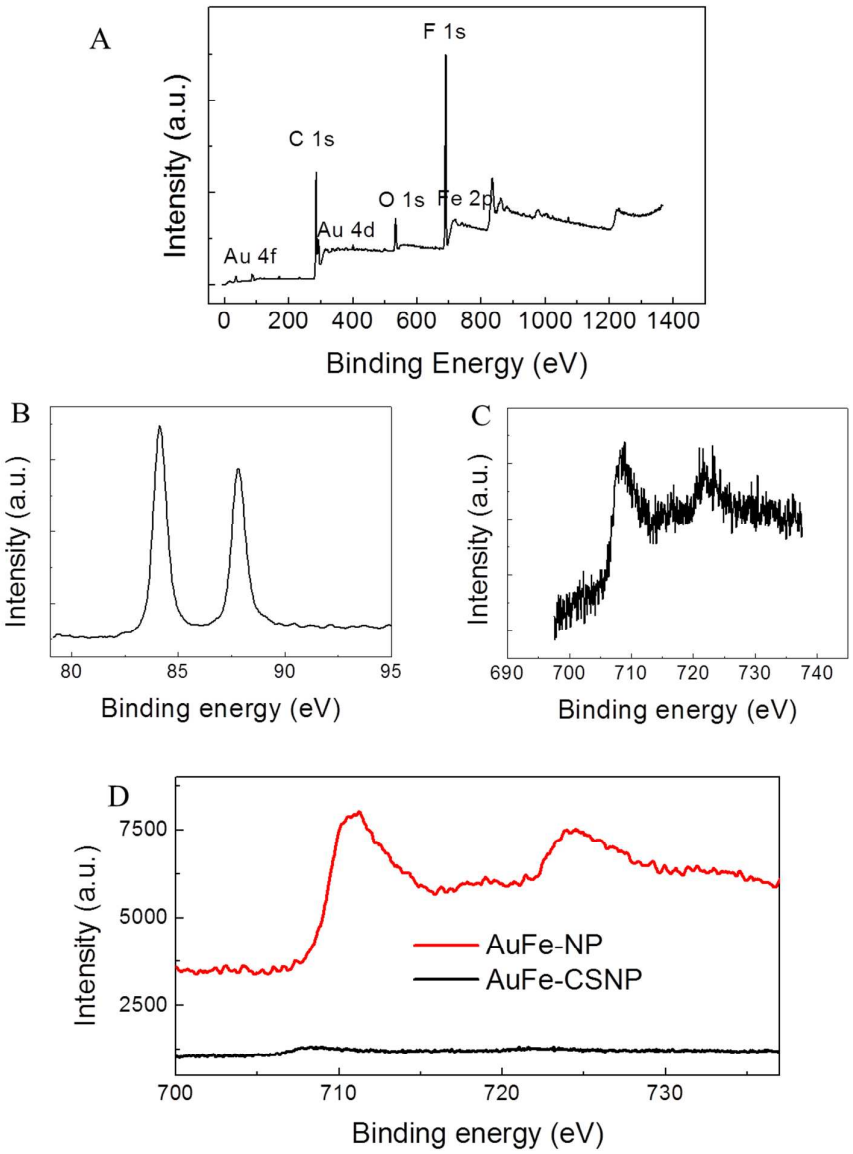

Figure S8. XPS spectra of AuFe-CSNPs. (A) full-range XPS spectrum; (B) Au 4*f* XPS spectrum; (C) Fe 3*d* XPS spectrum; (D) comparison of Fe 3*d* XPS spectra of AuFe-NP and AuFe-CSNP.

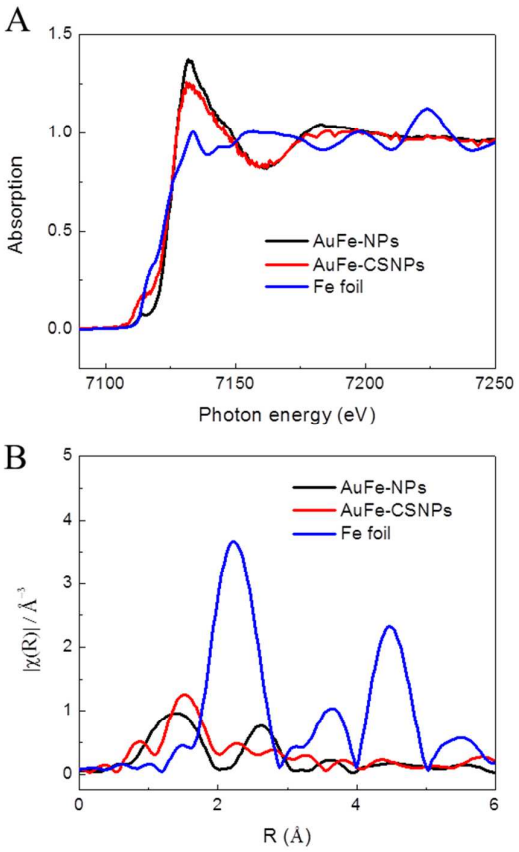

Figure S9. XAS Fe *K*-edge spectra of AuFe-NPs and AuFe-CSNPs. (A) XANES spectra, (B) FT-EXAFS spectra.

The Fe 3*d* XPS spectrum of the AuFe-CSNPs is very noisy (Figure S8C), suggesting a weak Fe intensity at the surface, as the Fe 3*d* XPS has an estimated probing depth of 1 nm. This is in agreement with the increased Fe concentration in electrolyte as observed by ICP-AES (Figure S6). We should note that the fluorescence mode of Fe K-edge is more bulk sensitive, and it likely has a better detection limit than that of Fe 3*d* XPS, thus the Fe K-edge spectrum for AuFe-CSNPs (Figure S9) is better than XPS spectrum for AuFe-CSNPs (Figure S8).

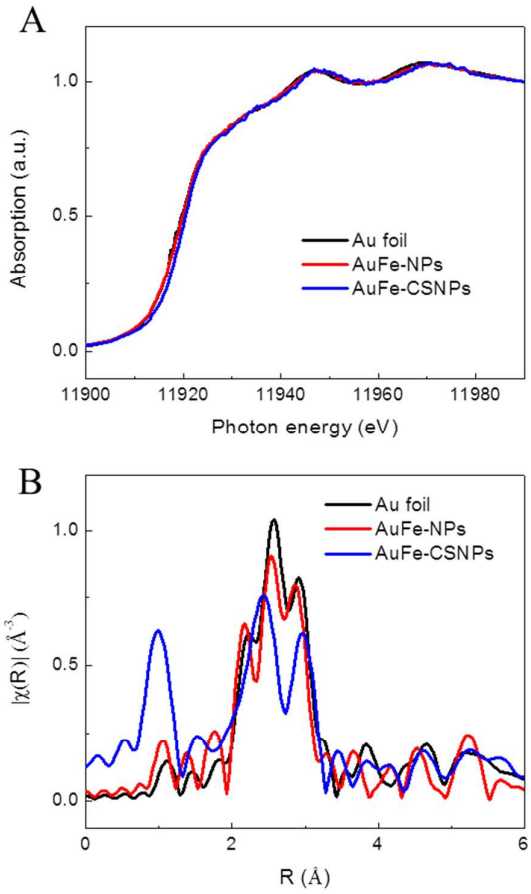

Figure S10. XAS Au L_3 spectra of Au element in AuFe-NPs and AuFe-CSNPs. (A) XANES spectra, (B) FT-EXAFS spectra.

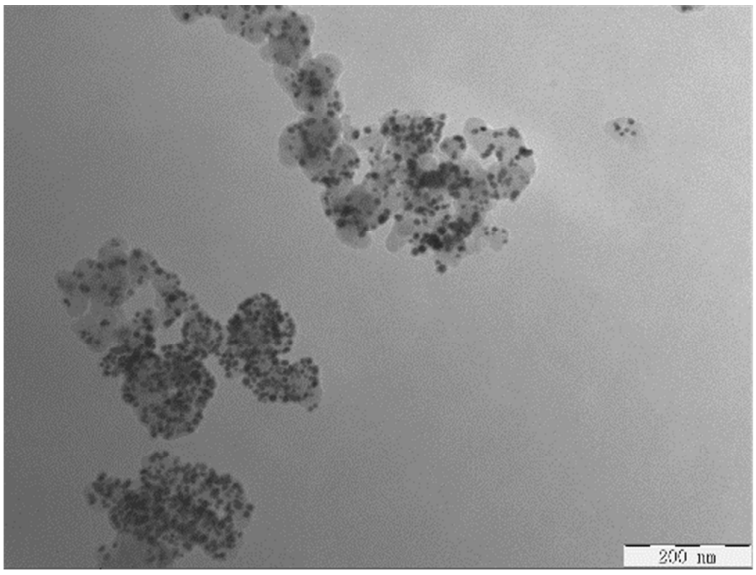

Figure S11. TEM image of Au NPs loaded on carbon black. These Au NP with a core diameter of ~8 nm. The distribution and loading density are similar with Au-Fe alloy NPs on carbon black. Scale bar is 200 nm.

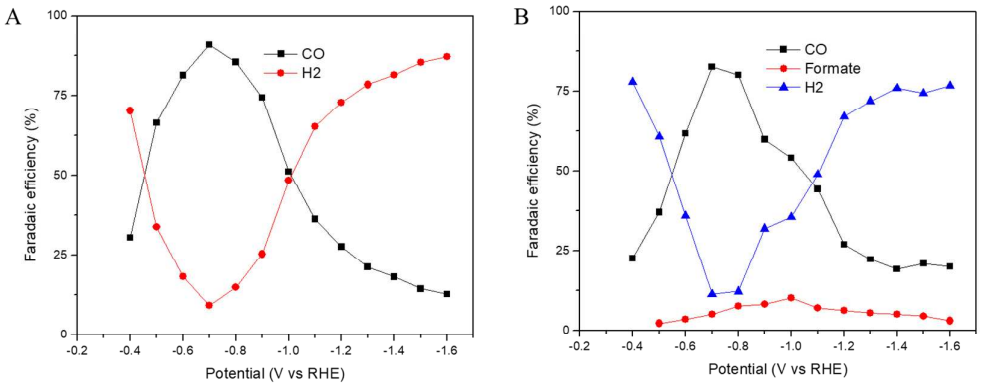

Figure S12. FE for each product as a function of potential on Au NPs (A) and Au foils (B).

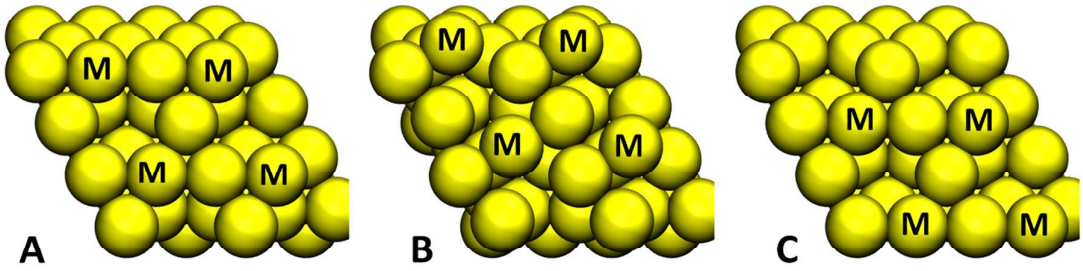

Figure S13. The diffusion pathway to calculate the diffusion barrier. (A) initial state, (B) transition state and (C) final state.

Supporting Tables

Table S1. Comparison of CO_2 reduction activity for Au-Fe alloy NPs with other catalysts. Mass activity was not reported by Refs R3, R5, R8. These noble metal-based nanostructures were prepared on foil. According to the surface feature and reduction activity, their mass activity was comparable to that of nanostructures in R6, but far lower than the value of 3 mA/mg.

Ref	Catalysts	Electrolyte & pH	Onset potential & FE	FE at -0.4V	Mass activity (mA/mg) at -0.4V
This work	Au-Fe NPs	0.5M $KHCO_3$ pH 7.2	-0.2 V 80%	97%	48.24
R1[10]	8 nm Au NPs	0.5M $KHCO_3$ pH 7.2	-0.37 V 22%	35%	0.5
R2[11]	500 nm long Au nanowires	0.5M $KHCO_3$ pH 7.2	-0.2 V 38%	91%	2.8
R3[12]	Oxide-derived Au NPs	0.5M $NaHCO_3$ pH 7.2	-0.2 V 10%	96%	N/A
R4[13]	Au Foil	0.5M $KHCO_3$ pH 7.2	-0.4 V 22.6%	22.6%	N/A
R5[14]	Au needles	0.5M $KHCO_3$ pH 7.2	-0.2 V 40%	＞95%	N/A
R6[15]	Nanoporous Ag	0.5M $KHCO_3$ pH 7.2	-0.2 V 3%	89%	0.20 (-0.5 V)
R7[16]	Ag NPs	0.5M $KHCO_3$ pH 7.2	-0.3 V 25%	48%	2.56 (-0.5 V)
R8[17]	Ag nano-corals	0.1M $KHCO_3$ pH 6.8	-0.4 V 76%	73%	N/A

Table S2. The calculated formation energies of *COOH ($E_{*\mathrm{COOH}}^{\mathrm{Formation}}$, in eV) the desorption energies of CO ($E_{\mathrm{CO}}^{\mathrm{Desorption}}$, in eV), the adsorption energies of *CO_2 ($E_{*\mathrm{CO2}}^{\mathrm{Adsorption}}$, in eV) and the adsorption energies of H* ($E_{*\mathrm{H}}^{\mathrm{Adsorption}}$, in eV). For pure Au, $E_{*\mathrm{COOH}}^{\mathrm{Formation}} = 0.50$ eV, $E_{\mathrm{CO}}^{\mathrm{Desorption}} = 0.21$ eV, $E_{*\mathrm{CO2}}^{\mathrm{Adsorption}} = -0.23$ eV and $E_{*\mathrm{H}}^{\mathrm{Adsorption}} = 0.11$ eV.

Metal	Sc	Ti	V	Cr	Mn	Fe	Co	Ni	Cu	Zn
$E_{*\mathrm{COOH}}^{\mathrm{Formation}}$	0.54	0.49	0.47	0.46	0.49	0.46	0.54	0.61	0.47	0.64
$E_{\mathrm{CO}}^{\mathrm{Desorption}}$	0.46	0.43	0.40	0.34	0.25	0.17	0.23	0.07	0.22	0.02
$E_{*\mathrm{CO_2}}^{\mathrm{Adsorption}}$	-0.27	-0.28	-0.28	-0.28	-0.28	-0.33	-0.27	-0.28	-0.27	-0.27
$E_{*\mathrm{H}}^{\mathrm{Adsorption}}$	0.22	0.18	0.20	0.20	0.22	0.13	0.20	0.17	0.04	0.15
Metal	Y	Zr	Nb	Mo	Tc	Ru	Rh	Pd	Ag	Cd
$E_{*\mathrm{COOH}}^{\mathrm{Formation}}$	0.52	0.47	0.43	0.41	0.47	0.55	0.56	0.64	0.55	0.59
$E_{\mathrm{CO}}^{\mathrm{Desorption}}$	0.43	0.52	0.43	0.29	0.29	0.25	0.27	0.11	0.14	0.30
$E_{*\mathrm{CO_2}}^{\mathrm{Adsorption}}$	-0.25	-0.28	-0.27	-0.28	-0.27	-0.27	-0.28	-0.27	-0.27	-0.26
$E_{*\mathrm{H}}^{\mathrm{Adsorption}}$	0.06	0.11	0.18	0.20	0.18	0.24	0.28	0.15	0.04	-0.05

References

1. Kresse, G.; Hafner, J., Ab Initio Molecular Dynamics for Liquid Metals. *Phys. Rev. B: Condens. Matter Mater. Phys.* **1993,** *47* (1), 558-561.
2. Kresse, G.; Furthmüller, J., Efficiency of Ab-initio Total Energy Calculations for Metals and Semiconductors Using a Plane-wave Basis Set. *Comput. Mater. Sci.* **1996,** *6* (1), 15-50.
3. Kresse, G.; Furthmüller, J., Efficient Iterative Schemes for Ab Initio Total-energy Calculations Using a Plane-wave Basis Set. *Phys. Rev. B: Condens. Matter Mater. Phys.* **1996,** *54* (16), 11169-11186.
4. Perdew, J. P.; Burke, K.; Ernzerhof, M., Generalized Gradient Approximation Made Simple. *Phys. Rev. Lett.* **1996,** *77* (18), 3865-3868.
5. Kresse, G.; Joubert, D., From ultrasoft pseudopotentials to the projector augmented-wave method. *Phys. Rev. B: Condens. Matter Mater. Phys.* **1999,** *59* (3), 1758-1775.
6. Grimme, S.; Antony, J.; Ehrlich, S.; Krieg, H., A Consistent and Accurate Ab Initio Parametrization of Density Functional Dispersion Correction (DFT-d) for the 94 Elements H-pu. *J. Chem. Phys.* **2010,** *132* (15), 154104.
7. Henkelman, G.; Uberuaga, B. P.; Jónsson, H., A climbing image nudged elastic band method for finding saddle points and minimum energy paths. *J. Chem. Phys.* **2000,** *113* (22), 9901-9904.
8. Sundararaman, R.; Goddard, W. A., The charge-asymmetric nonlocally determined local-electric (CANDLE) solvation model. *J. Chem. Phys.* **2015,** *142* (6), 064107.
9. Garrity, K. F.; Bennett, J. W.; Rabe, K. M.; Vanderbilt, D., Pseudopotentials for high-throughput DFT calculations. *Comput. Mater. Sci.* **2014,** *81*, 446-452.
10. Zhu, W.; Michalsky, R.; Metin, Ö.; Lv, H.; Guo, S.; Wright, C. J.; Sun, X.; Peterson, A. A.; Sun, S., Monodisperse Au Nanoparticles for Selective Electrocatalytic Reduction of CO2 to CO. *J. Am. Chem. Soc.* **2013,** *135* (45), 16833-16836.
11. Zhu, W.; Zhang, Y.-J.; Zhang, H.; Lv, H.; Li, Q.; Michalsky, R.; Peterson, A. A.; Sun, S., Active and Selective Conversion of CO2 to CO on Ultrathin Au Nanowires. *J. Am. Chem. Soc.* **2014,** *136* (46), 16132-16135.
12. Chen, Y.; Li, C. W.; Kanan, M. W., Aqueous CO2 Reduction at Very Low Overpotential on Oxide-Derived Au Nanoparticles. *J. Am. Chem. Soc.* **2012,** *134* (49), 19969-19972.
13. Hori, Y.; Kikuchi, K.; Suzuki, S., Production of CO and CH_4 in Electrochemical Reduction of CO_2 at Metal Electrodes in Aqueous Hydrogencarbonate Solution. *Chem. Lett.* **1985,** (11), 1695-1698.
14. Liu, M.; Pang, Y.; Zhang, B.; De Luna, P.; Voznyy, O.; Xu, J.; Zheng, X.; Dinh, C. T.; Fan, F.; Cao, C.; de Arquer, F. P. G.; Safaei, T. S.; Mepham, A.; Klinkova, A.; Kumacheva, E.; Filleter, T.; Sinton, D.; Kelley, S. O.; Sargent, E. H., Enhanced electrocatalytic CO2 reduction via field-induced reagent concentration. *Nature* **2016,** *537* (7620), 382-386.
15. Lu, Q.; Rosen, J.; Zhou, Y.; Hutchings, G. S.; Kimmel, Y. C.; Chen, J. G.; Jiao, F., A selective and efficient electrocatalyst for carbon dioxide reduction. *Nat. Commun.* **2014,** *5*, 3242.
16. Kim, C.; Jeon, H. S.; Eom, T.; Jee, M. S.; Kim, H.; Friend, C. M.; Min, B. K.; Hwang, Y. J., Achieving Selective and Efficient Electrocatalytic Activity for CO2 Reduction Using Immobilized Silver Nanoparticles. *J. Am. Chem. Soc.* **2015,** *137* (43), 13844-13850.
17. Hsieh, Y.-C.; Senanayake, S. D.; Zhang, Y.; Xu, W.; Polyansky, D. E., Effect of Chloride Anions on the Synthesis and Enhanced Catalytic Activity of Silver Nanocoral Electrodes for CO2 Electroreduction. *ACS Catal.* **2015,** *5* (9), 5349-5356.